

fronts within Boise sandstone was tracked experimentally and simulated successfully under a variety of injection modes and initial conditions<sup>13, 14</sup>.

This paper extends our foam displacement model to multidimensional, compositional, and nonisothermal reservoir simulation. For numerical stability and to accommodate the long time steps necessary for successful reservoir-scale simulation, a fully implicit backward-differencing scheme is used. The simulator employs saturation and surfactant concentration dependent rate expressions for lamella formation and destruction. Lamella mobilization is similarly included.

Our objectives are to show that not only is population-balance-based simulation of foam displacement possible in multidimensional heterogeneous porous media, but also highly instructive in regard to the physics of foam displacement. We consider geometrically simple, isothermal, oil-free systems. This allows easy comparison with our previous experimental and simulation results<sup>12, 13</sup>. Numerous verification exercises are performed to discover the role foam plays in gas displacement through zones of contrasting permeability and to highlight the interplay of foam-bubble texture and gas mobility.

**Foam in Porous Media.** Foam microstructure in porous media is unique<sup>15</sup>. Accordingly, to model gas mobility it is important to understand foamed-gas microstructure<sup>12</sup>. In water-wet porous media, the wetting surfactant solution remains continuous, and the gas phase is dispersed. Aqueous liquid completely occupies the smallest pore channels where it is held by strong capillary forces, coats pore walls in the gas-filled regions, and composes the lamellae separating individual gas bubbles. Only minimal amounts of liquid transport as lamellae. Most of the aqueous phase is carried through the small, completely liquid-filled channels. Gas bubbles flow through the largest, least resistive pore space while significant stationary bubbles reside in the intermediate-sized pore channels where the local pressure gradient is insufficient to sustain mobilized lamellae.

Foam reduces gas mobility in two manners. First, stationary or trapped foam blocks a large number of channels that otherwise carry gas. Gas tracer studies<sup>11, 16</sup> show that the fraction of gas trapped within a foam at steady state in sandstones is quite large and lies between 85 and 99%. Second, bubble trains within the flowing fraction encounter significant drag because of the presence of pore walls and constrictions, and because the gas/liquid interfacial area of a flowing bubble is constantly altered by viscous and capillary forces<sup>17, 18</sup>. Hence, foam mobility depends strongly on the fraction of gas trapped and on the texture or number density of foam bubbles.

Bubble trains are in a constant state of rearrangement by foam generation and destruction mechanisms<sup>15</sup>. Individual foam bubbles are molded and shaped by pore-level making and breaking processes that depend strongly on the porous medium<sup>9, 15</sup>. To account for foam texture in a mechanistic sense, foam generation and coalescence must be tracked directly. Additionally, bubble trains halt when the local pressure gradient is insufficient to keep them mobilized, and other trains then begin to flow. Bubble trains exist only on a time-averaged sense. More detailed summaries of the pore-

level distribution of foam, and the mechanisms controlling texture are given in refs. 12 and 15.

## Modeling Foam Displacement

A variety of empirical and theoretical methods for modeling foam displacement are available in the literature. These range from population-balance methods<sup>7, 8, 10, 11, 13, 19, 20</sup> to percolation models<sup>21-25</sup> and from applying so-called fractional flow theories<sup>26, 27</sup> to semi-empirical alteration of gas-phase mobilities<sup>1, 28-34</sup>. Of these four methods, only the population balance method and network or percolation models arise from first principles.

**Population-Balance Method.** The power of the population-balance method lies in addressing directly the evolution of foam texture and, in turn, reduction in gas mobility. Gas mobility is assessed from the concentration or texture of bubbles. Further, the method is mechanistic in that well-documented pore-level events are portrayed in foam generation, coalescence, and constitutive relations. Most importantly, the population balance provides a general framework where all the relevant physics of foam generation and transport may be expressed.

We chose the population-balance method because of its generality and because of the similarity of the equations to the usual mass and energy balances that comprise compositional reservoir simulation. Only a brief summary of the method is given here as considerable details of our implementation are available in the literature<sup>12-14</sup>.

The requisite material balance on chemical species  $i$  during multiphase flow in porous media is written as

$$\frac{\partial}{\partial t} \left[ \phi \sum_j (S_j C_{i,j} + \Gamma_{i,j}) \right] + \sum_j \nabla \cdot \mathbf{F}_{i,j} = \sum_j q_{i,j} \quad (1)$$

where  $\phi$  is the porosity,  $S$  is the saturation of phase  $j$ ,  $C$  is the molar concentration of species  $i$  in phase  $j$ ,  $\Gamma$  is the adsorption of species  $i$  from phase  $j$  in units of moles per void volume,  $\mathbf{F}$  is the vector of combined convective and diffusive flux of species  $i$  in phase  $j$ , and  $q$  is a rate of generation of  $i$  in phase  $j$  per unit volume of porous medium. To obtain the total mass of species  $i$ , we sum over all phases  $j$ .

In the foam bubble population balance,  $S_j n_f$  replaces  $S_j C_{i,j}$  where  $n_f$  is the number concentration or number density of foam bubbles per unit volume of flowing gas and  $S_f$  is the saturation of flowing gas. Hence, the first term of the time derivative is the rate at which flowing-foam texture becomes finer or coarser per unit rock volume. Since foam partitions into flowing and stationary portions,  $\Gamma$  becomes  $S_t n_t$  where  $S_t$  and  $n_t$  are the saturation of the stationary gas and the texture of the trapped foam per unit volume of trapped gas, respectively. Thus, the second term of the time derivative gives the net rate at which bubbles trap. Trapped and flowing foam saturation sum to the overall gas saturation,  $S_g = S_f + S_t$ . The second term on the left of Eq. (1) tracks the convection of foam bubbles where the flux,  $\mathbf{F}$ , is given by  $u_f n_f$ , and  $u_f$  is the Darcy velocity of the flowing foam. We neglect dispersion. Finally,  $q$  becomes the net rate of generation of foam bubbles. Within the above

framework, foam is a component of the gas phase and the physics of foam generation and transport become amenable to standard reservoir simulation practice.

The net rate of foam generation:

$$q_f = \phi S_g \left[ k_1 \left| \frac{\bar{v}_w}{\bar{v}_f} \right| \left| \frac{\bar{v}_f}{\bar{v}_f} \right|^{1/3} - k_{-1} \left| \frac{\bar{v}_f}{\bar{v}_f} \right| n_f \right] \quad (2)$$

is written per unit volume of gas. In the simulations to follow, we do not inject pregenerated foam and so we do not require a source/sink term for bubbles. Interstitial velocities, *i.e.*,  $\bar{v}_i = \bar{u}_i / \phi S_i$ , are local vector quantities that depend on the local saturation and total potential gradient, including gravity and capillary pressure. Foam generation is taken as a power-law expression that is proportional to the magnitude of the flux of surfactant solution multiplied by the 1/3 power of the magnitude of the interstitial gas velocity. The liquid-velocity dependence originates from the net imposed liquid flow through pores occupied by both gas and liquid, whereas the gas-velocity dependence arises from the time for a newly formed lens to exit a pore<sup>35</sup>. Snap-off is sensibly independent of surfactant properties consistent with its mechanical origin<sup>15</sup>. The proportionality constant reflects the number of foam germination sites. Intuitively, the number of snap-off sites falls with decreasing liquid saturation. However,  $k_1$  is taken as a constant here. The generation rate expression does vary implicitly with liquid saturation through the gas and liquid velocities.

To prevent coalescence of newly formed gas bubbles, a surfactant must stabilize the gas/liquid interface. Foam lamellae form given sufficient suction capillary pressure and a stabilizing surfactant. However, too high of a suction-capillary pressure will overcome the stabilizing influence of surfactant and collapse a lamella<sup>15</sup>. A flowing lamella is vulnerable to breakage in termination sites as it flows into a divergent pore space where it is stretched rapidly. If sufficient time does not elapse for surfactant solution to flow into a lamella and heal it, coalescence ensues<sup>36</sup>.

Equation (2) shows that foam lamellae are destroyed in proportion to the magnitude of their interstitial flux,  $v_f n_f$ , into such termination sites. The coalescence rate constant,  $k_{-1}$ , varies strongly with the local capillary pressure and surfactant formulation. It is given by

$$k_{-1} = k_{-1}^o \left( \frac{P_c}{P_c^* - P_c} \right)^2, \quad (3)$$

where the scaling factor,  $k_{-1}^o$  is taken as a constant and  $P_c^*$  is the limiting capillary pressure for foam coalescence<sup>37</sup>.

The "limiting capillary pressure,"  $P_c^*$ , as identified by Khatib *et al.*<sup>37</sup>, refers to the characteristic value of capillary pressure that a porous medium approaches during strong foam flow. It is set primarily by surfactant formulation and concentration. Highly concentrated foamer solutions and robust surfactants lead to a high  $P_c^*$ . In situations where surfactant transport is transient, we expect  $P_c^*$  to vary locally with surfactant concentration. The experimental work of Aronson *et al.*<sup>38</sup> suggests the following functional form for  $P_c^*$  versus surfactant concentration of robust foamer solutions:

$$P_c^* = P_{c,\max}^* \left( \frac{C_s}{C_s^o} \right) \quad (4)$$

where  $P_{c,\max}^*$  is a limiting value for  $P_c^*$  and  $C_s^o$  is a reference surfactant concentration for strong net foam generation.

In the simulations of heterogeneous porous media to follow, we assume that  $P_c^*$  is independent of absolute permeability. Foam-lamella coalescence is determined mainly by the rupture capillary pressure of isolated lamellae which, in turn is set by the concentration and type of surfactant, and not the nature the porous medium<sup>36</sup>. Equations (3) and (4) correctly predict that at high capillary pressures or for ineffective foamer solutions  $k_{-1}$  is quite high<sup>37, 38</sup>. The foam coalescence rate approaches infinity as the porous medium capillary pressure approaches  $P_c^*$ . We also assume geometric similarity between layers of differing permeability. Thus, for a uniform liquid saturation in the heterogeneous medium, foam is more vulnerable to breakage in the low permeability zones because  $P_c$  scales inversely as the square root of the absolute permeability according to the Leverett J-function<sup>39</sup>.

In addition to bubble kinetic expressions, the mass balance statements for chemical species demand constitutive relationships for the convection of foam and wetting liquid phases. Darcy's law is retained, including standard multiphase relative permeability functions. However, for flowing foam, we replace the gas viscosity with an effective viscosity relation for foam. Since flowing gas bubbles lay down thin lubricating films of wetting liquid on pore walls, they do not exhibit a Newtonian viscosity. We adopt an effective viscosity relation that increases foam effective viscosity as texture increases, but is also shear thinning

$$\mu_f = \mu_g + \frac{\alpha n_f}{\left| \frac{\bar{v}_f}{\bar{v}_f} \right|^{1/3}} \quad (5)$$

where  $\alpha$  is a constant of proportionality dependent mainly upon the surfactant system. In the limit of no flowing foam we recover the gas viscosity. This relation is consistent with the classical result of Bretherton<sup>40</sup> for slow bubble flow in capillary tubes (see also, refs. 17, 18, 41, 42).

Finally, stationary foam blocks large portions of the cross-sectional area available for gas flow and, thus must be accounted for to determine gas flux. Since the portion of gas that actually flows partitions selectively into the largest, least resistive flow channels, we adopt a "Stone-type" relative permeability model<sup>43</sup> that, along with effective viscosity, specifies gas-phase flow resistance. Because wetting aqueous liquid flows in the smallest pore space, its relative permeability is unaffected by the presence of flowing and stationary foam in accordance with the experimental results of refs. 44-48. Since flowing foam partitions selectively into the largest pore space, the relative permeability of the nonwetting flowing gas is a function of only  $S_f$ . Consequently, gas mobility is much reduced in comparison to an unfoamed gas propagating through a porous medium, because the fraction of gas flowing at any instant is quite small<sup>11, 16</sup>.

## Compositional Foam Simulator

Our starting point for multidimensional foam simulation is M<sup>2</sup>NOTS (Multiphase Multicomponent Nonisothermal Organics Transport Simulator), a nonisothermal, n-component, compositional simulator capable of handling three-phase flow in response to viscous, gravity, and capillary forces<sup>42</sup>. It is a compositional extension of TOUGH2<sup>43, 44</sup> and uses the integral finite difference method (IFDM) to discretize the flow domain (*cf.*, ref. 52).

Spatial gradients are calculated in a manner identical to the classic block-centered finite difference method. Flow mobilities are upstream weighted except for the absolute permeability between blocks of differing permeability. These are based on harmonic weighting.

A cubic equation of state represents the thermodynamic properties of the gas phase, which for nitrogen gas at the temperatures and pressures simulated here reduces to an ideal gas. The method of corresponding states describes the oil phase. The International Steam Tables provide the properties of the aqueous phase<sup>45</sup>. The simulator has been used successfully to model the deposition and clean up of petroleum hydrocarbons from soils and groundwater<sup>42</sup>.

We treat foam bubbles as a nonchemical component of the gas phase. Thus, the additional transport equation for foam-bubble texture described above is added to the mass balances for water, gas, and n organic components. The discretized foam-bubble equation is fully implicit with upstream weighting of the gas-phase mobility consistent with all other chemical species. Surfactant is simply an organic component that is highly soluble in water. In each grid block, the magnitude of the vectors representing the interstitial gas and liquid velocities are used to compute foam generation and coalescence rates from Eq. (2). The magnitude of each velocity is obtained by first summing the flow of each phase into and out of a grid block in the three orthogonal directions. Then the arithmetic average for each direction is calculated and the magnitude of the resultant vector used to calculate foam generation and coalescence rates. The gas velocity is similarly computed for the shear-thinning portion of the foam effective viscosity.

Numerical values of the population balance parameters are determined from steady-state measurements in one-dimensional linear flow. Steady-state flow trends, saturation, and pressure drop profiles are matched. These can all be obtained within one experimental run. The suite of foam displacement parameters do not need to be adjusted to accommodate different types of transient injection or initial conditions. Parameter values used here are taken from ref. 13 and apply specifically to very strong foams in the absence of oil and under isothermal conditions.

## Numerical Model Results

Because there are numerous initial conditions, modes of injection, and multidimensional geometries of interest, we present the results from several carefully chosen illustrative examples. First, we compare simulator predictions against experimental results for the simultaneous injection of nitrogen and foamer solution into a linear core presaturated with surfactant solution. Second, foam flow in heterogeneous, noncommunicating and communicating

linear layers is considered. The layers are again assumed to be presaturated with surfactant. Next, we simulate the one-dimensional radial flow of foam and consider two different initial conditions. In one case, the porous medium is initially free of surfactant, while in the following case, it is initially saturated with surfactant solution. Here, we focus on the evolution of gas mobility as foam flows outward radially. Finally, we present simulations of surfactant and gas coinjection into a 2.5-acre five-spot pattern that is initially free of surfactant. To avoid confusion between foam formation, surfactant propagation and adsorption, foam-oil interaction, and partitioning of surfactant into the oil phase, we choose a porous medium that does not adsorb surfactant and never contains any oil. In all simulations, the rock is initially filled with the aqueous phase,  $S_w = 1$ . Nitrogen and foamer solution are coinjected simultaneously. Thus, we focus attention on foam formation, coalescence, transport, and reduction of gas mobility.

**Linear Core.** In the first example, nitrogen is injected continuously into a linear core of length 0.60 m at a rate of 0.43 m/day relative to the exit pressure of 4.8 MPa. Foamer solution is also injected continuously at 0.046 m/day to give a quality or gas fractional flow of 0.90 at the core exit. The medium is initially filled with surfactant solution. These flow rates and initial conditions correspond exactly to our previous experiments conducted in a 1.3-d Boise sandstone with a length of 0.60 m<sup>12, 13</sup>. The foamer is a saline solution (0.83 wt% NaCl) with 0.83 wt% active Bioterg AS-40, a C<sub>14-16</sub> alpha olefin sulfonate, available from Stepan Chemical Company.

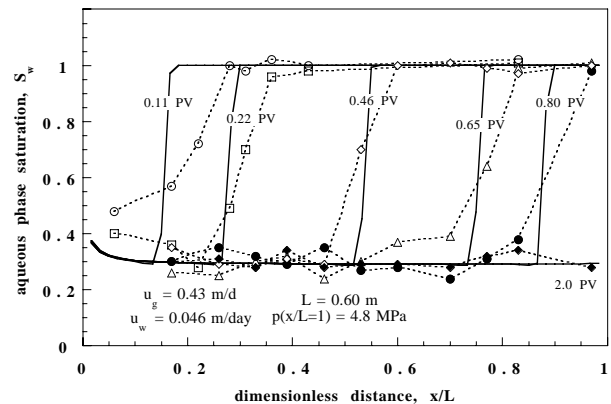


**Fig. 1—Experimental and model transient aqueous-phase saturation profiles for 1-d displacement.**

**Figures 1 and 2** display the transient experimental and simulated saturation and pressure profiles, respectively. **Figure 3** displays the foam texture profiles. Theoretical results are represented by solid lines. Dashed lines simply connect the individual data points. Elapsed time is given as pore volumes of total fluid injected, that is, as the ratio of total volumetric flow rate at exit conditions multiplied by time and divided by the core void volume.

Steep saturation fronts are measured and predicted at all time levels in **Fig. 1** whereby aqueous-phase saturation upstream of the front is roughly 30% and downstream it is

100%. Model fronts are somewhat steeper and sharper than those measured experimentally, but the theoretical saturation profiles track experimental results very well. From the saturation profiles it is apparent that foam moves through the core in a piston-like fashion. Note that the simulation displays little numerical dispersion.

Even though nitrogen and surfactant solution are injected separately, rapid foam generation and liquid desaturation occur at the core inlet. A region of net foam generation near the inlet is clearly evident in the transient pressure profiles of **Fig. 2**. Both the experiments and calculations show that pressure gradients near the inlet are shallow, indicating that flow resistance is small and foam textures are coarse consistent with the injection of unfoamed gas. Steep pressure gradients are found downstream of the inlet region. These steep pressure gradients confirm the existence of a strong foam piston-like front moving through the core.

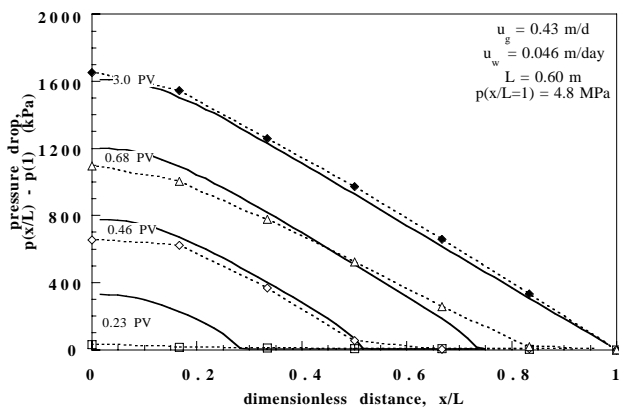


**Fig. 2—Experimental and model transient pressure profiles for 1-d displacement.**

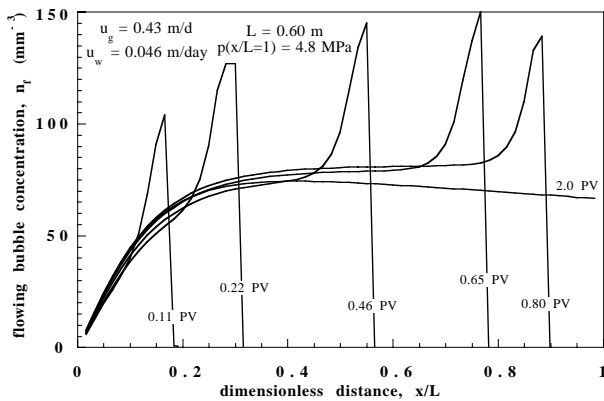


**Fig. 3—Model transient flowing-foam texture profiles for 1-d displacement.**

**Figure 3** reports the predicted foam texture as a function of dimensionless distance and time. We find a coarsely textured foam near the inlet. Beyond the first fifth of the core, foam texture becomes very fine and nearly constant at each time level until it rises and peaks immediately before the front. High pressure gradients and fine foam textures are seen where liquid saturation is low and *vice versa*. No method currently exists to measure *in situ* foam texture

directly. However, the predicted effluent bubble textures do match the bubble size of foams exiting a similar Berea sandstone<sup>9, 19</sup>.

One interesting feature of **Fig. 3** is the elevation of foam texture near the foam front above that in steady-state and also that immediately upstream of the foam front. This feature is more pronounced here than in our previous modeling work<sup>12, 13</sup>. The difference occurs because of the switch from an IMPES (implicit pressure explicit saturation) method with explicit upstream weighting of fluid mobilities to a fully implicit scheme. Physically, foam texture is fine at the foam front because the aqueous-phase saturation increases from roughly 0.30 to 1. For high aqueous-phase saturation, Eq. (3) gives a very low foam coalescence rate. At the same time, interstitial liquid and gas rates are high resulting in a large rate of net foam generation. Setting Eq. (2) to zero and solving for the value of the local equilibrium foam texture indeed shows that texture can be quite high at the foam front. Because this intensive foam generation is confined to a very small region, pressure gradients at the foam front are affected negligibly, as displayed in **Fig. 2**. Further, as this result appears to be physical, we make no attempt to suppress it.

Gas compressibility effects are also found in **Fig. 3**. At steady state, the foam texture decreases along the latter portion of the of the core. As they flow downstream, the small compressible foam bubbles find themselves out of equilibrium with the lower pressure. Consequently, bubbles expand increasing their velocity. This increased velocity triggers increased foam coalescence and a more coarsely textured foam. Gas compressibility similarly accounts for foam textures finer than the steady-state texture upstream of the foam fronts at time levels of 0.65 and 0.80 PV.

In addition to good agreement with experiment, the model results in **Figs. 1 to 3** agree quite well with our previous calculations<sup>13</sup>. Again, the foam displacement parameters employed here and in the previous work are identical. In the remaining simulations, we assume that the fraction of gas flowing in the presence of foam is a constant equal to 0.10. This shortens the computation time required for multidimensional calculations by decreasing the stiffness of the equations. The impact of the increase in foam texture at the foam front on gas mobility is also moderated.

**Heterogeneous Noncommunicating Linear Layers.** In this section, we consider the case of two linear layers with different permeabilities and without cross flow. Both layers are initially filled with foamer solution as in the previous case. This geometry applies to a reservoir with continuous impermeable shale breaks and to parallel core experiments in the laboratory. The high permeability layer is assigned a permeability of 1.3 d which is identical to the permeability of the Boise sandstone cores used in our laboratory<sup>12, 13</sup>. The permeability of the second layer is made a factor of 10 smaller, 0.13 d. Each layer is assumed to be geometrically similar and is given the same porosity, Leverett J-function<sup>39</sup>, and relative permeability functions. Initially, both layers are saturated with aqueous surfactant solution. Superficial velocities maintained in these simulations are the same as in the linear corefloods portrayed in **Figs. 1 - 3**. The system length is set at 0.60 m to allow direct

comparison with these corefloods. Continuity of pressure is maintained at the inlet and outlet. Otherwise, each layer accepts whatever portion of the injected fluids it desires.

It is useful to begin by considering the effect that foam has on reappportioning the production from each layer. **Figure 4** displays as solid lines the fraction of the original water displaced from each layer as a function of the time. The small amounts of surfactant solution injected with the gas are not included in the produced volume. Time is again given nondimensionally by the total pore volumes injected. Also, injection of nitrogen at 0.48 m/day in the absence of surfactant is shown with dashed lines as a reference case. For the unfoamed gas injection, little liquid is produced from the low permeability layer. Although the displacement of water from the high permeability layer is initially rapid, gas quickly moves through the 1.3-d layer and the production rate declines after only 0.2 PV. Nitrogen is very mobile relative to water making it an exceptionally poor displacement fluid. Foaming the nitrogen has a dramatic effect. Production from both layers is maintained for about a pore volume of injection indicating that foam provides efficient displacement in both the high and low permeability layers. Production stops at 1 PV because the displacement is essentially complete in 1 PV.

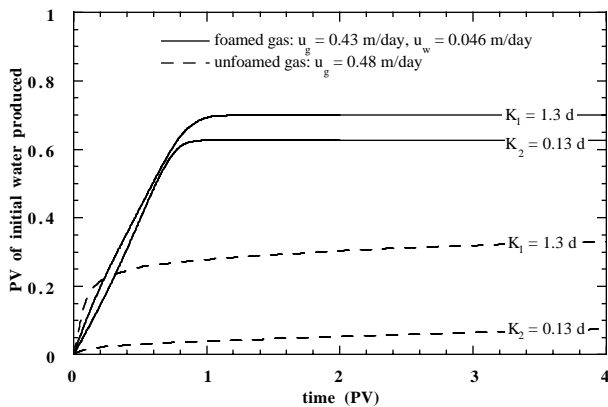
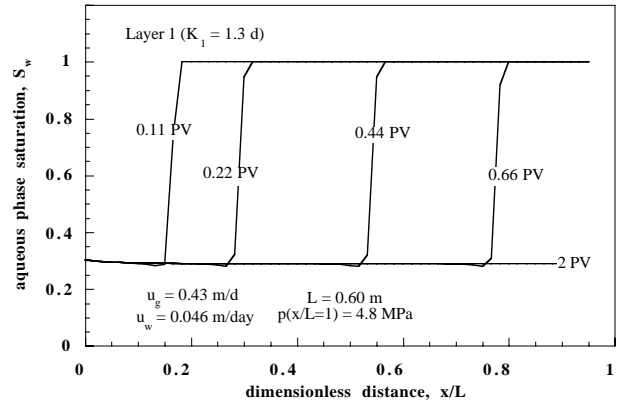


**Fig. 4—Fraction of the initial water displaced by foamed gas and unfoamed gas as a function of time from two isolated layers.**

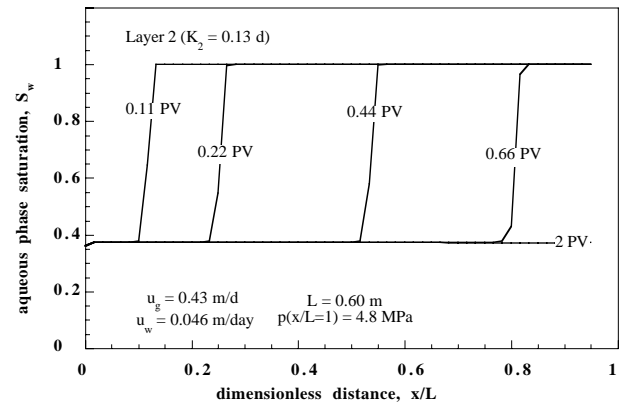
The improvement of diversion with foam is seen quite strikingly in **Fig. 5** which gives the simulated saturation profiles in each layer as a function of time. In the high-permeability-layer saturation profile shown in **Fig. 5a**, the foam front initially moves more quickly than in the low permeability layer as illustrated in **Fig 5b**. However, at 0.44 PV the foam displacement fronts in each layer are positioned at approximately  $x/L$  equal to 0.55. By examining the displacement fronts at 0.66 PV, we find that the front in the low permeability layer is actually ahead of the front in the high permeability layer. Foam breakthrough occurs first in the low permeability layer. Again, these are very efficient displacements because we began with the porous medium saturated with surfactant solution and use strong foam displacement parameters characteristic of AOS 1416 in oil-free porous media.

Another interesting feature of **Fig. 5** is the steady-state aqueous-phase saturation in each layer. Because the layers

are isolated, the strong foam generated in each layer causes the capillary pressure of each layer to approach  $P_c^*$ . The aqueous-phase saturation at steady state in each layer is thus set by  $P_c^*$ , and the steady-state saturations are related by  $P_c^*$  through the Leverett J-function<sup>37</sup>. Hence, the 0.13-d layer only desaturates to an  $S_w$  of about 0.38 before the limiting capillary pressure is approached, whereas in the 1.3-d layer, the  $S_w$  at steady state is 0.30.



**(5a)**



**(5b)**

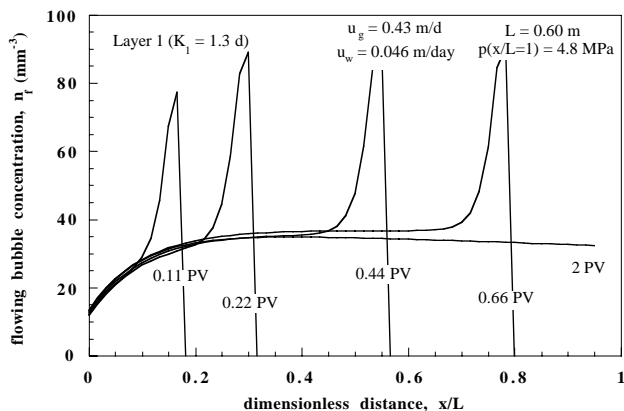
**Fig. 5—Transient aqueous-phase saturation profiles for displacement from two isolated layers.**

Saturation profiles in **Fig. 5** are best understood by considering the foam texture in each layer. A finely textured foam forms in the high permeability layer, as portrayed in **Fig. 6a** leading to substantial flow resistance. Conversely, the foam that is generated in the lower permeability layer shown in **Fig. 6b**, is over an order of magnitude coarser. Accordingly, the low permeability layer presents an overall flow resistance comparable with that of the high permeability layer. Roughly half of the entire gas flow is diverted to the 0.13-d layer.

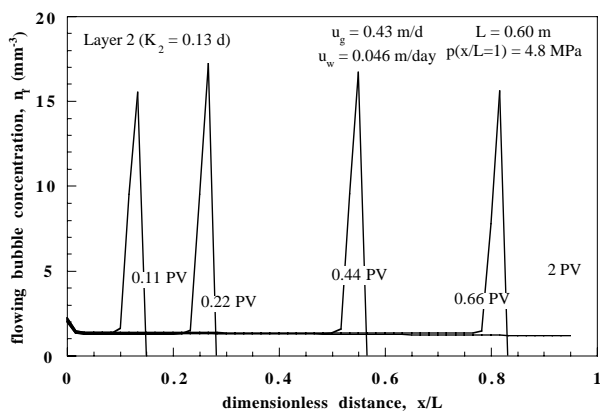
**Figure 7** presents the companion pressure-drop information for simultaneous injection of nitrogen and foamer solution into isolated layers of differing permeability. Pressure gradients build quickly in both layers consistent with the rapid foam generation displayed in **Fig. 6**. Interestingly, the total system pressure drop is only 2/3 of that found in the one-dimensional linear flow of **Fig. 2** at

these same superficial velocities. Because the foam texture in both layers of Fig. 6 is substantially less than that predicted in Fig. 3 for one-dimensional flow, flow resistance and pressure drop are significantly less.

Comparison of Fig. 7 with the saturation and bubble texture profiles in Figs. 5 and 6 shows that saturation, bubble texture, and pressure fronts track exactly as they did in one-dimensional linear flow. Where foam texture is large,  $S_w$  is low, pressure gradients are large, and *vice versa*.



(6a)



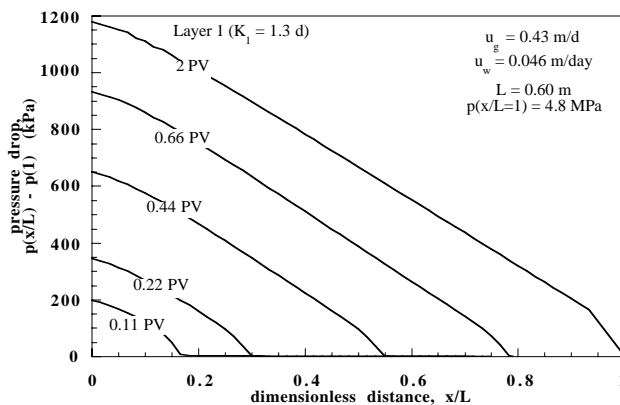
(6b)

Fig. 6—Transient flow-foam textures for displacement from two isolated layers.

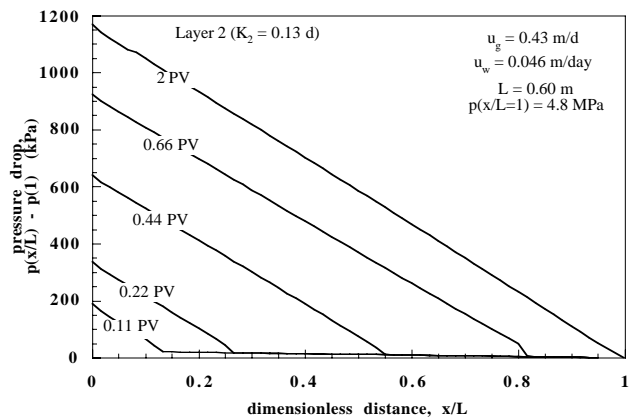
**Heterogeneous Communicating Linear Layers.** The geometry, initial conditions, and flow rates employed here are identical to those for the noncommunicating linear layer case. However, cross-flow between the layers is allowed. Figure 8 contrasts production of the original aqueous-phase fluid from each layer when foam is both present (solid lines) and absent (dashed lines). Again, we find that foam induces significant production from the low permeability zone compared to gas injection. Displacement in both layers is quite efficient.

Figure 9 shows that sharp saturation fronts propagate at equal rates in both layers. Since the layers are communicating, gas at the foam front minimizes its flow resistance. For example, when the local flow resistance in the 1.3-d layer rises, some portion the foamed gas diverts

into the 0.13-d layer, and *vice versa* yielding equal propagation rates in each layer. Saturation fronts in each layer are, thus, bound together by the necessity to maintain the minimum flow resistance. Likewise, this is true for unfoamed gas. The striking feature of Fig. 9 is the efficiency of displacement in each layer.



(7a)



(7b)

Fig. 7—Transient pressure profiles for displacement from two isolated layers.

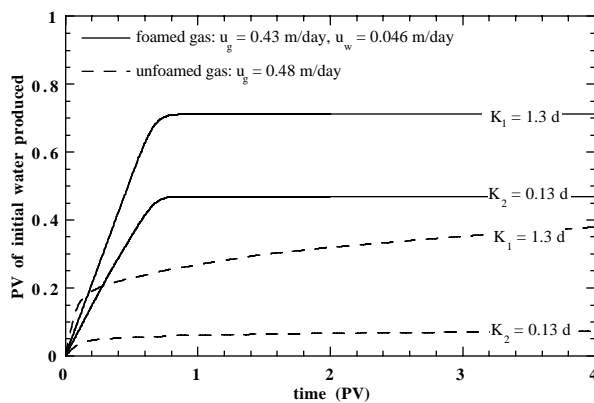
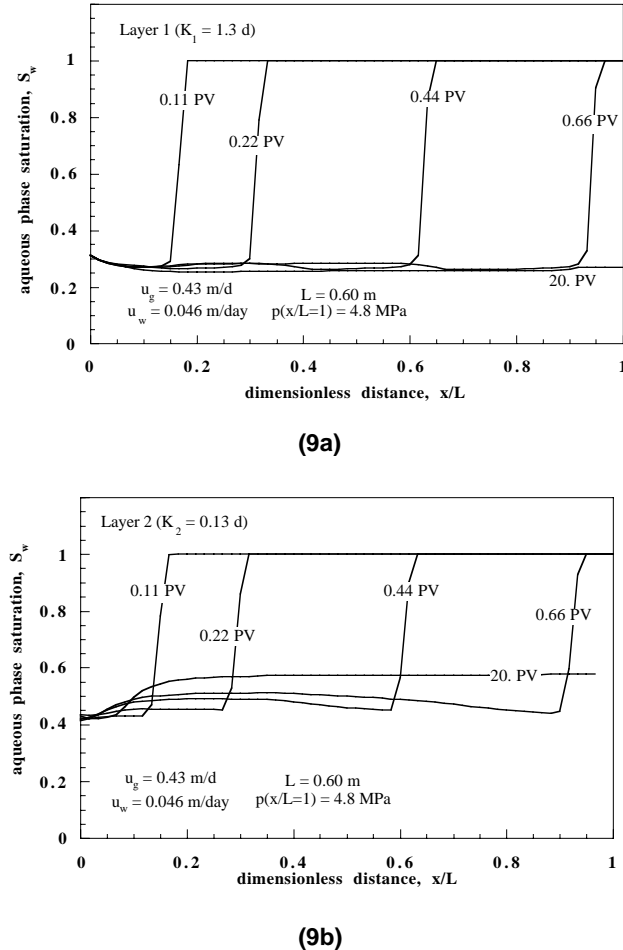


Fig. 8— Fraction of the initial water displaced by foamed gas and unfoamed gas as a function of time from two isolated layers.

Prior to foam breakthrough,  $S_w$  upstream of the saturation front in the low permeability, 0.13-d layer is larger in **Fig. 9b** than it is in **Fig. 5b** for noncommunicating layers. During foam propagation, each layer attempts to come to the  $S_w$  corresponding to the limiting capillary pressure. Because there is cross-flow and capillary connection between the layers, water is drawn into the low permeability layer maintaining  $S_w$  at slightly higher levels than in the noncommunicating layers of **Fig. 5b**.



**Fig. 9—Transient aqueous-phase saturation profiles for displacement from two communicating layers.**

Foam breakthrough occurs just after 0.66 PV. After breakthrough, the aqueous-phase saturation in the high permeability layer remains constant at about 0.27. In the low permeability layer, however,  $S_w$  slowly increases over time. At 20 PV the average aqueous phase saturation downstream of the inlet is 0.58. The lower permeability layer slowly refills with water in an attempt to come into capillary equilibrium with the high permeability layer where the capillary pressure is much lower. Equilibrium is achieved when  $S_w$  reaches roughly 0.87 everywhere in the low permeability layer.

Refilling of the 0.13-d layer with foamer solution has a dramatic effect on the foam texture over time, as shown in **Fig. 10b**. Prior to foam breakthrough, foam textures are comparable with those found in the previous cases. At 0.22 PV the bubble density in the low permeability layer

averages about  $30 \text{ mm}^{-3}$  in the foam-filled region. After breakthrough and as the layer refills with water in order to reduce its capillary pressure, the rate of foam coalescence decreases with decreasing capillary pressure as indicated by Eq. (3). Consequently, the net rate of foam generation increases according to Eq. (2) as does the flowing bubble texture. The average bubble texture between 0.66 PV and 10 PV increases by a factor of nearly 3.5. Increasing textures indicate increasing flow resistance. As flow resistance increases, the gas flow rate and also the foam coalescence rate decrease exacerbating the growth in foam texture. The texture in the high permeability layer shown in **Fig. 10a** is relatively coarse in obedience with the large foam coalescence rates caused by the high capillary pressure there and the relatively high gas flow rates. The texture becomes coarser with time because the high permeability layer carries increasingly more gas that in turn increases foam coalescence in the 1.3-d layer. In the meantime, the lower permeability layer fills with foam. The refilling effect is unlikely to be encountered in practical application of foam since it only occurs after many PV of foam injection.

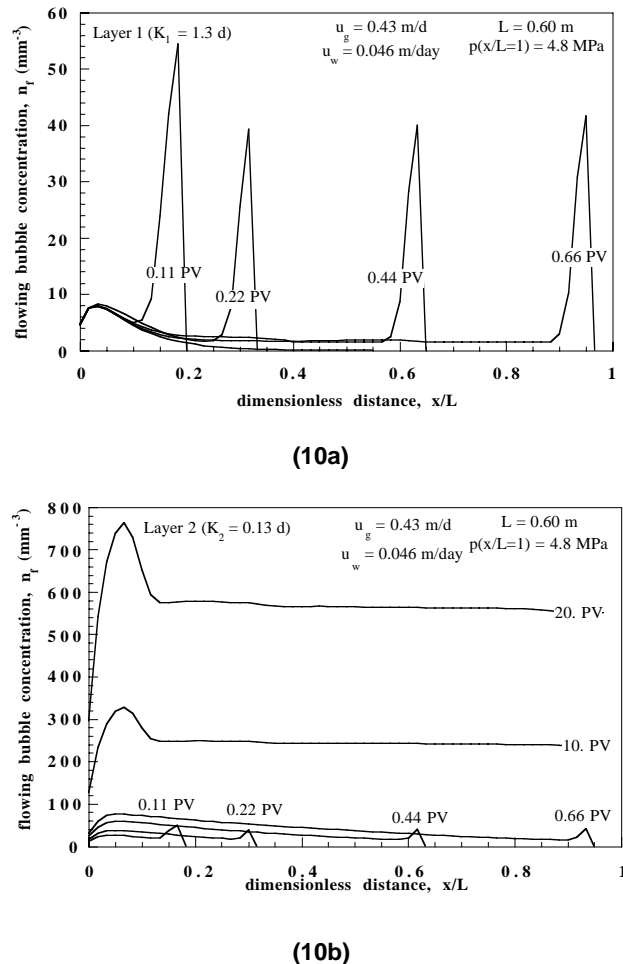
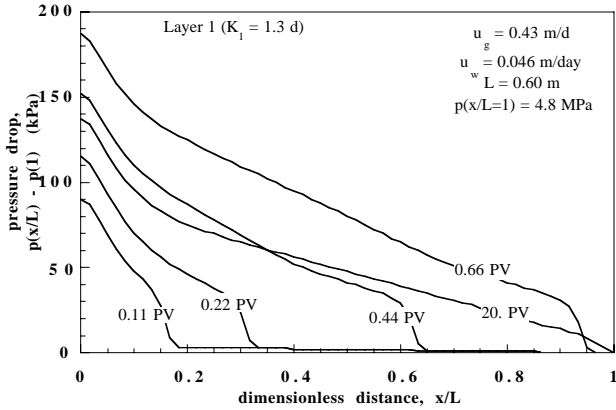


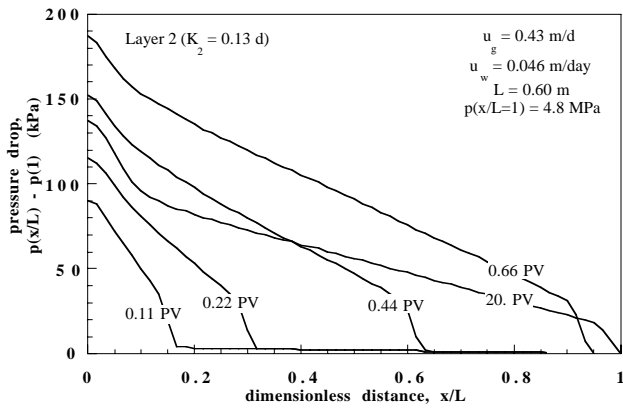
**Fig. 10— Transient flow-foam textures for displacement from two communicating layers.**

The pressure drop profiles shown in **Fig. 11** contain several additional interesting features. First, note the magnitude of the pressure drops. The maximum pressure

drop displayed is roughly 200 kPa (22 psi), whereas the identical flow rate conditions in **Fig. 2** yielded a steady state pressure drop of a little more than 1600 kPa (230 psi). The flow resistance in the 1.3-d layer is small because foam is coarsely textured there and because the gas superficial velocity is large exploiting the shear-thinning foam rheology. This commands a smaller net flow resistance than that found in the linear one-dimensional and noncommunicating layer cases. Second, the pressure drop declines in time as the foam coarsens in the high permeability layer. The system pressure drop at 0.66 PV is nearly 190 kPa while at 20 PV it has declined to 140 kPa.



(11a)



(11b)

**Fig. 11—Transient pressure profiles for displacement from two communicating layers.**

**Radial Flow.** Next, we consider simultaneous injection of nitrogen and foamer solution into a radial, one-dimensional, homogeneous porous medium that is 1 m thick with a radius,  $R$ , of 71.5 m and a permeability of 1.3 d. The medium is initially saturated with surfactant-free brine. Volumetric injection rates are  $0.165 \text{ m}^3/\text{day}$  of surfactant solution and  $3.14 \text{ m}^3/\text{day}$  of nitrogen relative to the 4.8 MPa backpressure to give a gas fractional flow of 0.95.

**Figure 12** displays the radial aqueous-phase saturation profiles as a function of time. Dimensionless radial distance is simply  $r' = (r - r_{well})/R$ . At short times (e.g., 0.1 PV), two saturation fronts exist. The front that has

propagated farthest into the medium corresponds to unfoamed gas. For the 0.1 PV saturation profile, this first front is at roughly  $r' = 0.7$ . Little liquid is displaced by this front because gas mobility is high in the absence of foam. The trailing front is quite steep, sharp, and indicates efficient displacement. It arises because of foam generation and propagation. Behind these strong foam fronts,  $S_w$  is only about 5 saturation units above connate saturation. The velocity of both fronts slows as they move outward radially, as expected. Further, foam front propagation is slow because it can move only as quickly as surfactant propagates.

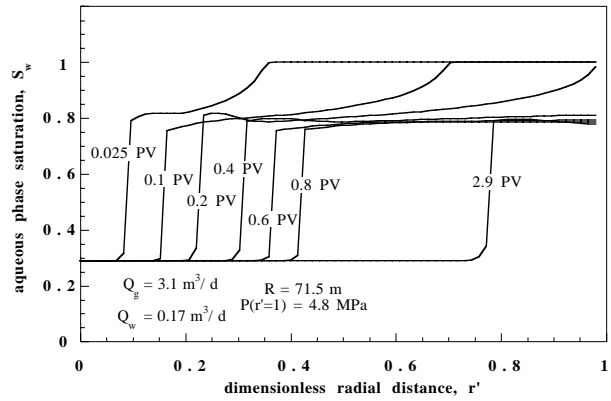


**Fig. 12—Transient aqueous-phase saturation profiles for the radial flow of foam and surfactant.**

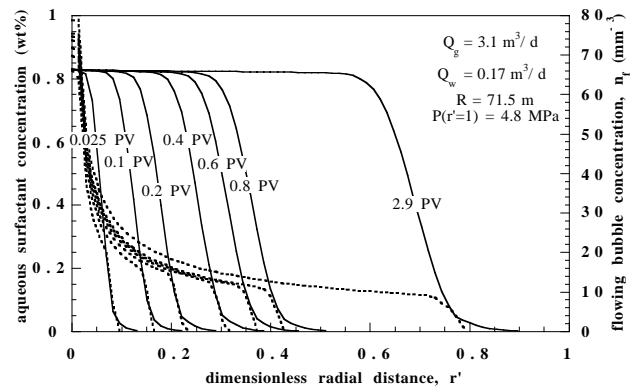


**Fig. 13—Transient flowing-foam texture profiles superimposed upon surfactant concentration profiles for the radial flow of foam.**

This point is better illustrated in **Fig. 13** which presents the transient bubble concentration profiles superimposed over the surfactant concentration profiles. Foam texture is presented with a dashed line and bubble concentrations are located on the right y-axis. Surfactant concentration in weight percent is given with a solid line and values are found on the left y-axis. Foam texture is fine close to the injector, but texture falls off quickly as foam moves out radially and the gas and liquid velocities fall off as  $1/r$ . Foam texture abruptly where the surfactant concentration falls to zero, because  $P^*_c$  approaches zero in the absence of surfactant and the foam coalescence rate

approaches infinity. Ahead of the surfactant front, a continuous channel of unfoamed gas exists. It is interesting to compare the bubble profiles in **Fig. 13** with the previous three cases, **Figs. 3, 7, and 10**. In the earlier examples, foam textures immediately behind the foam fronts are elevated above the steady-state value and above the textures found farther upstream. Since there was ample surfactant at the front due to presaturation, stable foam films were generated; since the capillary pressure at the front is relatively low, the foam coalescence rate is low. In the radial case shown in **Fig. 13**, there is no elevation in the foam texture immediately behind the foam front. Here, the foam coalescence rate is relatively high. The surfactant concentration decreases to zero across the foam front leading to low  $P_c^*$  at the front according to Eq. (4) and to large foam coalescence rates according to Eq. (3).

**Figure 14** shows the radial pressure profiles as a function of time on a semi-logarithmic scale. Pressure drop initially builds quickly in time as foam generates and fills the region around the injection well. The rate of pressure increase declines with time as the foam propagation rate slows in outward radial flow. Pressure gradients near the injection point are shallow just as they are for linear flow in **Fig. 2**. Because the radial grid is relatively coarse (72 grid blocks) compared to the radial distance spanned (*i.e.*, 72 m), the change in pressure gradient near  $r'$  equal to 0.02 is abrupt. Little foam is present in the first grid block making flow resistance small. Away from the inlet region, the pressure gradient declines as  $1/r$  similar to a Newtonian fluid. Apparent Newtonian behavior is maintained because foam texture falls off as foam flows in the  $r$ -direction as shown in **Fig. 13**.

Tremendous pressure drops are predicted in **Fig. 14**, consistent with the foam-displacement parameters used to match our linear core floods (**Fig. 2**). These are incredibly strong foams reflecting the high limiting capillary pressures of AOS 1416 at concentrations around 1 wt% in the absence of oil. Practical field implementation of foam requires careful selection of the foaming agent and concentration<sup>54</sup>. Recall, that **Figs. 6 and 11** predict that pressure drops should decrease in heterogeneous environments.

Patzek and Koinis<sup>1</sup> reported mobility reduction factors (MRF = gas mobility / foam mobility) inferred from the Kern River steam-foam pilots, that decreased steadily with increasing distance from the injection well<sup>1</sup>. **Figure 15** shows this same trend for our foam simulations. The predicted MRF decreases with increasing radial distance from the injector. Although the foam displacement simulated here is shear thinning at constant texture, we find that the MRF must decrease consonant with the decreasing foam textures of **Fig. 13**. In radial flow, the decrease of foam texture with increased distance has a greater effect on gas mobility than shear-thinning in Eq. (5). Again, high MRF is predicted because we employ parameters and initial conditions in the foam displacement simulator that give strong, efficient foams. In the steam-foam field tests, the gas fractional flow was very high and gravity override was significant leading to dry foams that were very vulnerable to coalescence forces and hence much more coarse in texture. Additionally, heat losses that cause steam condensation, surfactant losses due to adsorption and precipitation, and foam coalescence due to the presence of oil were

significant. All of these factors lessen the impact that foam has on gas mobility.

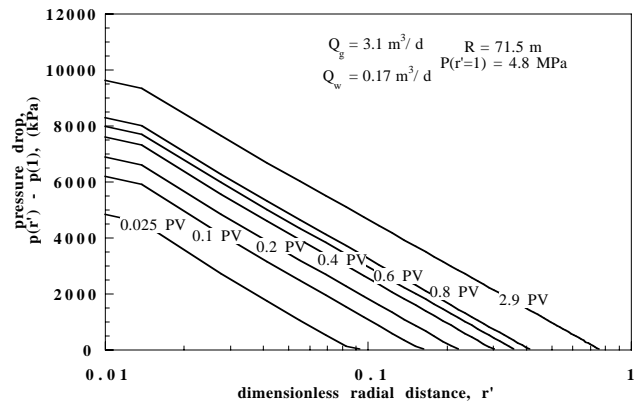


**Fig. 14**—Transient pressure profiles for the radial flow of foam and surfactant.

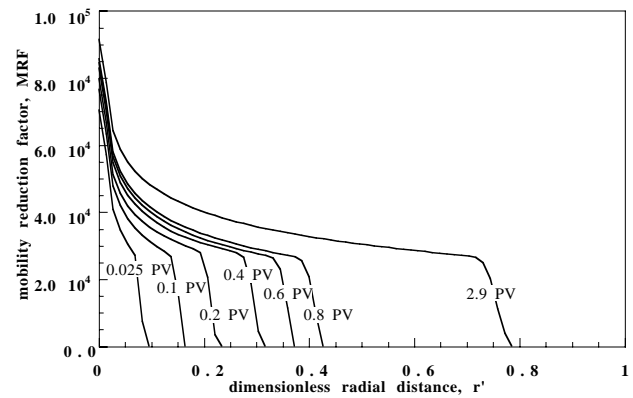


**Fig. 15**—Transient mobility reduction factors for the transient flow of foam and surfactant.

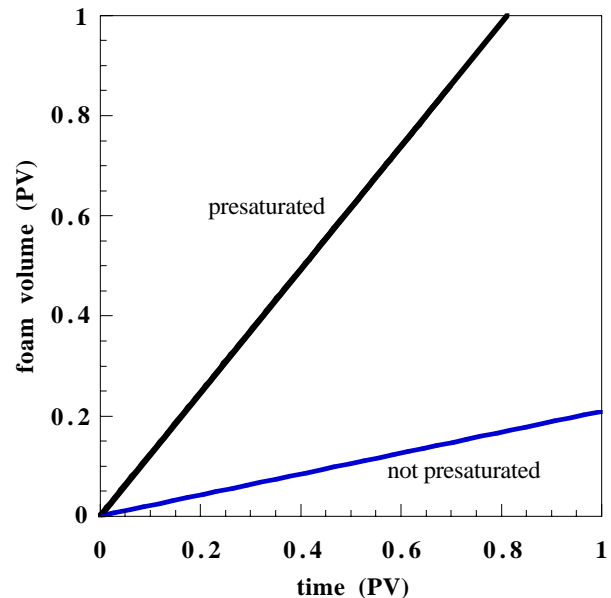


**Fig. 16**—Volume of foam in place versus total fluid injection (compare to **Fig. 13** of ref 1).

Another interesting comparison to the results reported by Patzek and Koinis<sup>1</sup> is given in **Fig. 16**. Radial foam growth rate is displayed by plotting *in-situ* foam volume in PV as a function of the total cumulative fluid injection, relative the system backpressure of 4.8 MPa. Results garnered from the present case are shown as well as those from a radial simulation at identical injection rates and conditions except that the medium has been preflushed with surfactant. Both curves reveal that the PV of foam in place increases linearly with the total injected PV. Qualitatively, this trend agrees with that observed in steam-foam field studies where foam propagated in proportion to the injected PV of surfactant solution. The slope of the presaturated case demonstrates how efficient foam displacement might be in the absence of rock adsorption and foam-oil interaction under conditions of coinjection of gas and foamer solution.

**5 Spot.** The final case is simultaneous injection into one quarter of a confined 5-spot pattern. Hence, we simulate diverging/converging flow. The formation is assumed to be 20 m thick, the injector to producer spacing is 72 m, and the formation is not dipping. These dimensions correspond

roughly to the conditions of the Mecca steam-foam pilot so that we may continue our qualitative comparisons to documented field results. The simulation assumes that the formation is homogeneous with a permeability of 1.3 d, is initially filled with brine, and is bounded by impermeable layers. Injection occurs across the bottom 1/8 of the formation, whereas the producer is completed across the entire interval and is maintained at a pressure of 4.8 MPa. We present saturation, bubble texture, and surfactant concentration profiles in the vertical cross section between injector and producer. Grid spacing is 2 m in the horizontal direction and 1 m in the vertical direction.

To provide contrast with the highly efficient foam displacement to follow, we first ran simulations of unfoamed gas injection. Gas saturation contours in the vertical cross section are presented in **Fig. 17** at 50, 100, 200 and 300 d. The gray-scale shading indicates the gas saturation. Unshaded portions of the graph refer to an  $S_g$  of zero, and progressively darker shading corresponds to larger  $S_g$ . Without foam, areas contacted by gas are poorly swept. Buoyancy quickly drives injected gas to the top of the formation, a gas tongue forms, and gas breakthrough at the producer occurs quite quickly.

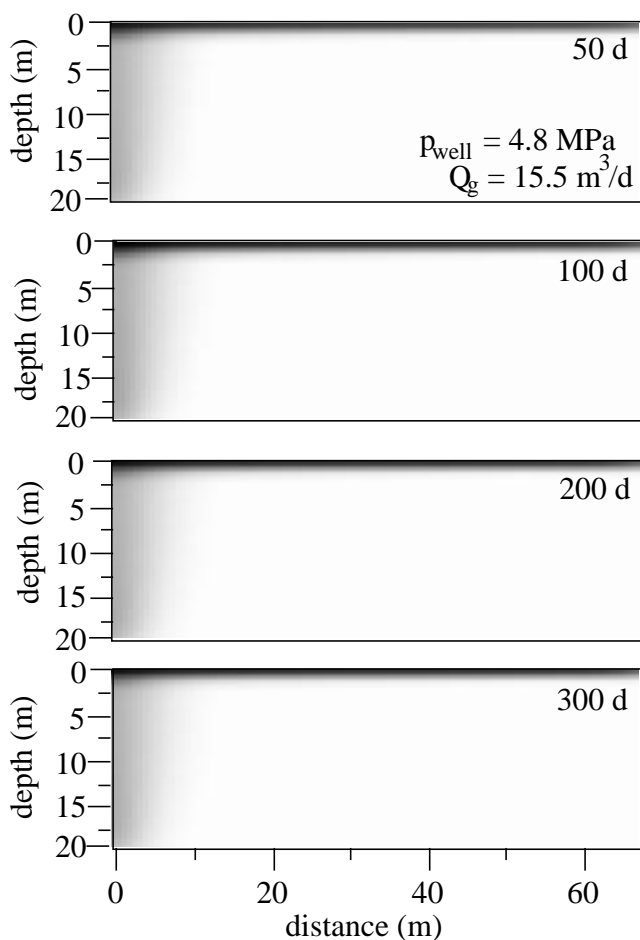


**Fig. 17**—Gas saturation profiles for unfoamed gas injection into a confined 5 spot.

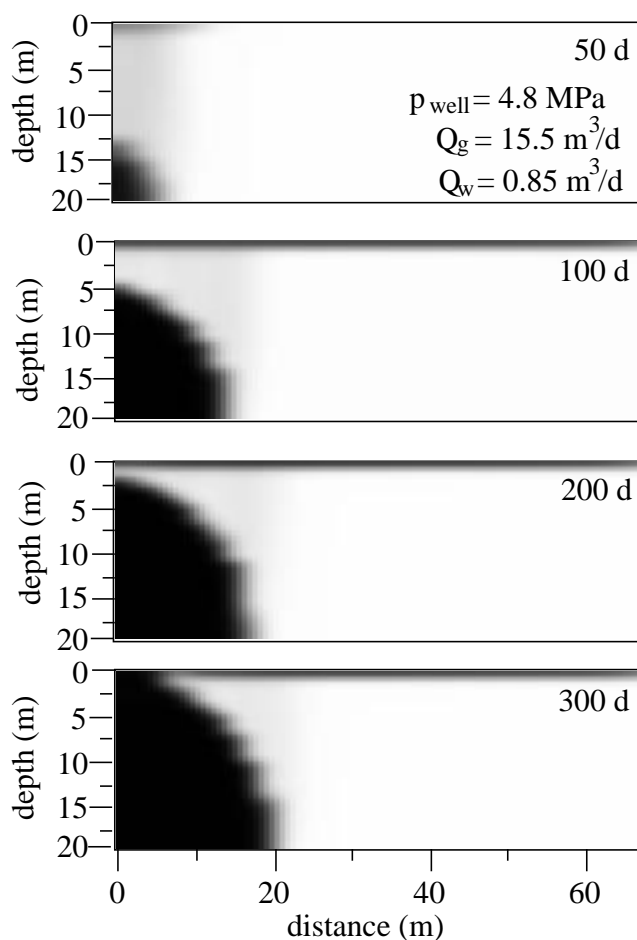


**Fig. 18**—Gas saturation profiles for the simultaneous injection of gas and foamer solution into a confined 5 spot.

After breakthrough, little desaturation occurs because pressure gradients are low and buoyancy prevents gas from contacting areas along the lower horizontal boundary. This is classical gravity override.

With simultaneous injection of  $N_2$  and 0.83 wt% foamer solution, foam generates where surfactant and gas are present, and the results are dramatically different. **Figures 18, 19, and 20** present  $S_g$ ,  $n_f$ , and  $C_s$  profiles respectively, in the vertical cross section at times of 50, 100, 200, and 300 days. The gas fractional flow is identical to the radial case, 0.95. Injection rates for  $N_2$  and aqueous solution are 15.5 and 0.85  $m^3/d$ , respectively. In **Fig. 18**, the gas saturation contours indicate that both a strong displacement by foam is occurring and a weak displacement by the unfoamed gas ahead of the foam front in a fashion similar to the radial displacement in **Fig. 12**. Near the injector, the high gas saturation region associated with the foamed gas assumes a semi-spherical shape. The contours at later times in **Fig. 18** illustrate that spherical growth and efficient displacement continue. The darkly shaded region immediately below the upper impermeable boundary indicates a tongue of unfoamed gas that forms due to

gravity override. Although not depicted, areal sweep is also good where foam is present.

**Figure 19** illustrates foam texture as a function of time. The foamed regions correspond exactly with zones of high gas saturation. The bubble textures associated with black shading are  $100 \text{ mm}^{-3}$ , and the light-gray shading at the foam front is roughly  $20 \text{ mm}^{-3}$ . Interestingly, and in agreement with **Fig. 13**, the most finely textured foams are found adjacent to the well bore where gas and liquid flow velocities are largest.

The most provocative result of this simulation is found in **Fig. 20**: surfactant is actually lifted in the formation above its injection point. Black shading indicates a concentration of 0.83 wt%. Foamed gas effectively desaturates the zone around the injector. Although the aqueous-phase relative permeability function is unchanged in the presence of foam, the low  $S_w$  results in low relative permeability and highly resistive flow for the aqueous phase. The flow of surfactant-laden water is rerouted and surfactant is pushed upward in the formation. In this example, gravity override has been effectively negated.

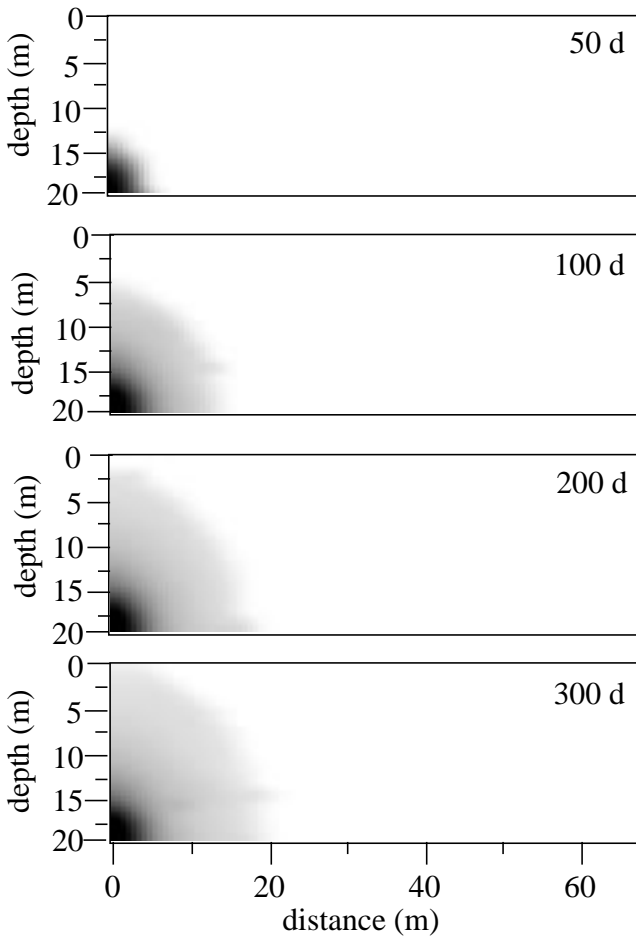


**Fig. 19**—Foam texture profiles for the simultaneous injection of gas and foamer solution into a confined 5 spot.

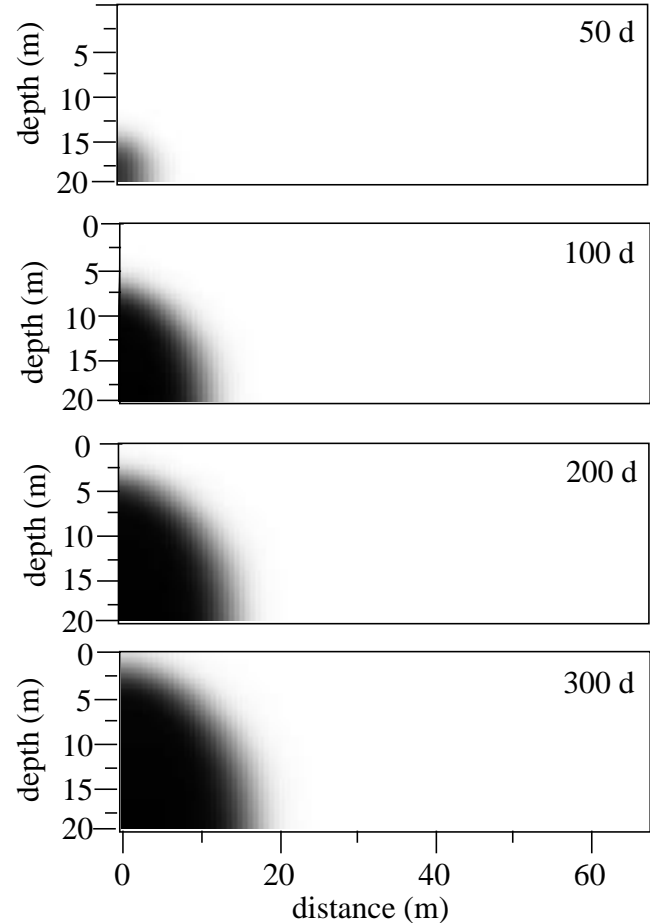


**Fig. 20**—Surfactant concentration profiles for the simultaneous injection of gas and foamer solution into a confined 5 spot.

When foam reaches the upper boundary of the layer, displacement continues from left to right in the horizontal direction in a piston-like fashion that expels the resident liquid phase. Propagation is slow until the flow begins to converge.

## Discussion

Recently, Rossen and coworkers<sup>26,27</sup> presented a fractional-flow theory for foam displacement in porous media. Their approach is notable since they consider gas diversion by foam among layers of differing permeability. Beginning with the steady-state experimental observations that aqueous-phase relative permeability is unchanged from the foam-free case<sup>44-48, 55</sup> and that aqueous-phase saturation is virtually constant<sup>9, 56</sup> they use Darcy's law, as illustrated by Khatib *et al.*<sup>37</sup> and Persoff *et al.*<sup>56</sup>, to obtain a fractional-flow theory for gas mobility in the presence of foam. This method does not explicitly account for the role that foam texture plays in reducing gas mobility. Additionally, the method is not readily applied to two- and three-dimensional flow. It does address, however, radial flow, diversion among isolated layers of differing permeability, and layers in capillary equilibrium.

Our simulations of layered porous media presaturated with surfactant solution reveal that significant flow diversion and production from low permeability layers occurs regardless of whether the layers communicate or not. For practical applications, the extent of diversion into low permeability layers predicted by our population-balance model is quite different than the prediction of the fractional flow theory of Rossen *et al.*<sup>26, 27</sup>. Because the fractional-flow model sets the capillary pressure in each layer equal to  $P_c^*$  at all times, it predicts strong foams in the low permeability layer and diversion into the high permeability layer. This asymptotic behavior is seen in **Fig 10b** as finely textured foam evolves in the low permeability layer because of the low coalescence rate at high water saturation and low  $P_c$  there. However, this behavior occurs only after more than 1 PV of foam has been injected, an occurrence unlikely to happen in the field. We should caution here that the foam textures predicted after many pore volumes of injection in **Fig. 10b** are exceptionally fine. When bubbles become so closely spaced, we expect foam generation by snap-off to cease as the close spacing of the bubbles prevents sufficient liquid accumulation for snap-off<sup>7</sup>.

For radial flow, our population balance method predicts that foam texture and, consequently, MRF falls with increasing distance from the injection well in both steady and unsteady flow consistent with field observations of gas mobility<sup>1</sup>. The fractional-flow model for foam, though, predicts that MRF is independent of radial distance. In the fractional flow model, all of the effects of foam on gas mobility are inferred from the wetting liquid mobility which is nearly constant for foam flow at the limiting capillary pressure. Since we explicitly account for the coarsening of foam texture as foam flows radially and the effect that texture has on gas mobility, we are able to obtain trends qualitatively similar to those observed in the field.

The case of simultaneous foamer and gas injection into a 5-spot geometry also permits some comparison with field trends. Firstly, we are able to simulate the propagation of foam far into the reservoir and improved vertical sweep<sup>1, 4</sup>.

Secondly, there is some evidence for spherical growth of the foam zone, such as that shown in **Fig. 19**, in the Kern River steam-foam pilots<sup>1</sup>. We predict a constant growth rate of the foam zone, just as was found in the field. Likewise, temperature observations collected at the pilots indicate foam zones with roughly spherical shape.

The calculations presented in this paper represent only a small fraction of the interesting cases possible. Since we specified that all porous media were initially free of oil, we discovered the effect that foam might have if strong foam generation occurred *in situ*. We have not included coalescence terms for the interaction of foam with oil. Although our simulator is fully capable of modeling steam injection, we have not simulated such cases. Additionally, there is speculation of a minimum pressure gradient required to propagate foams under field conditions<sup>3, 21-24</sup>. We have not simulated foam including such a mobilization pressure gradient.

Only the effects of strong foam were simulated here. By simulating a surfactant system with a smaller  $P_c^*$ , it is possible to simulate weak foams that can display even more interesting diversion behavior. For example, if  $P_c^*$  is less than the capillary entry pressure of a porous medium, foam will not form<sup>37</sup>. Hence, stable foam may be generated in high permeability layers where the capillary entry pressure is slightly lower than  $P_c^*$  but not at all in low permeability layers. Flow resistance in the high-permeability layer will thus be significant and will divert substantial gas flow into the foam-free low-permeability layer. Further, gravitational effects and the interplay with heterogeneity should be considered more closely. Gravity might cause the top of a reservoir to be so dry that only very weak foams subject to rapid coalescence can form or the rock may be so dry that no foam formation is possible. Finally, we need to simulate steam foams for which condensation is important.

Hence, we caution that the results shown here are not general. Foam displacement in porous media depends strongly on bubble texture which is influenced through the limiting capillary pressure by foamer formulation including the type of surfactant, surfactant concentration, the concentration and type of ions in solution, as well as the temperature. In all cases presented here, displacements begin with the formation full of water. High water saturation and low capillary pressure are conducive to foam formation. Different initial and injection conditions might change the effectiveness of foam as a displacement agent. Likewise, our knowledge of foam trapping is not sufficient to predict whether trapping occurs to the same degree, and in the same fashion, in high and low permeability rocks, even if geometrically similar.

## Summary

We have shown that it is practical to model foam displacement mechanistically in multidimensions. Beginning with an n-component compositional simulator, the bubble population-balance equations are successfully incorporated within the simulator's fully implicit framework. The mechanistic population-balance approach allows us to insert the physics of foam displacement directly into a reservoir simulator. Foam is treated as a nonchemical "component" of the gas phase and the evolution of foam texture is modeled explicitly through

pore-level foam generation and coalescence equations. As foam mechanisms become better understood, this framework allows for their inclusion.

For both noncommunicating and communicating linear heterogeneous layers, foamed gas efficiently diverts to low permeability layers when the layers are initially saturated with surfactant solution in the absence of gravity. For communicating layers, the foam propagation rate is equal in both layers. In this instance, foam dramatically evens out injection profiles.

For one-dimensional radial flow, we find that foam pressure drop scales as  $1/r$  similar to a Newtonian fluid. The gas mobility reduction factor for radial foam flow falls off as foam moves outward radially from the injector because the foam coarsens. This decline in mobility reduction factor in radial flow is consistent with previous field observations of steam-foam propagation<sup>1</sup>.

For simultaneous injection of gas and foamer solution into a confined 5-spot pattern, we clearly see two displacement fronts. Unfoamed gas moves upward through the formation due to buoyancy and is ineffective in displacement. The second front tracks with surfactant propagation and the generation of foam. The strong foam desaturation front takes a semi-spherical shape for short times with the origin of the sphere at the injector. Importantly, it is found that gravity override can be effectively negated.

These predictions are a result of the direct approach taken to model foam displacement. Since gas mobility in the presence of foam depends strongly on foam texture, it is necessary to account for foam-bubble evolution to model gas mobility generally and correctly.

## Nomenclature

$C$	= concentration
$F$	= component vector flux,
$k$	= rate constant
$K$	= permeability
$L$	= length of linear porous medium
MRF	= mobility reduction factor
$n$	= number density of foam
$p$	= pressure
$P_c$	= capillary pressure
PV	= pore volume (injected or in place)
$q$	= generation rate and source/sink term
$r$	= radial distance
$R$	= radial extent of porous medium
$S$	= phase saturation
$t$	= time
$u$	= Darcy velocity
$v$	= interstitial velocity

## Greek Letters

$\alpha$	= proportionality constant for foam effective viscosity
$\nabla \cdot$	= divergence operator
$\phi$	= porosity
$\mu$	= viscosity
$\Gamma$	= adsorption isotherm

## Subscripts

1	= generation rate constant
-1	= coalescence rate constant
$f$	= flowing foam

$g$	= gas phase
$i$	= phase ( <i>i.e.</i> , aqueous, gas, or oil)
$j$	= chemical species
$s$	= surfactant
$t$	= stationary foam
$w$	= water or wetting phase
$wc$	= connate water saturation
$well$	= denotes well radius

## Superscripts

$o$	= denotes reference value
$*$	= value corresponds to the limiting capillary pressure
$\bar{\quad}$	= denotes normalized radial distance

## Acknowledgement

This work was supported by the Assistant Secretary for Fossil Energy, Office of Oil, Gas, and Shale Technologies of the U. S. Department of Energy, under contract No. DE-ACO3-76FS00098 to the Lawrence Berkeley National Laboratory of the University of California and under contract No. DE-FG22-96BC14994 to Stanford University.

## References

1. Patzek, T.W. and M.T. Koinis: "Kern River Steam-Foam Pilots," *JPT*, **42**(4) (1990) 496-503.
2. Djabbarah, N.F., S.L. Weber, and D.C. Freeman: "Laboratory Design and Field Demonstration of Steam Diversion with Foam," SPE 20067, Proceedings of the 60th California Regional Meeting, Ventura, CA (April 1990).
3. Friedmann, F., M.E. Smith, W.R. Guice, J.M. Gump, and D.G. Nelson: "Steam-Foam Mechanistic Field Trial in the Midway-Sunset Field," *SPE*, **9**(4) (1994) 297-304.
4. Mohammadi, S.S., D.C. Van Slyke, and B.L. Ganong: "Steam-Foam Pilot Project in Dome-Tumbador, Midway-Sunset Field," *SPE*, **4**(1) (1989) 7-16.
5. Svorstøl, I., F. Vassenden, and K. Mannhardt: "Laboratory Studies for Design of a Foam Pilot in the Snorre Field," SPE 35400, Proceedings of the SPE/DOE 10th Symposium on Improved Oil Recovery, Tulsa, OK (1996).
6. Aare, M.G. and A. Skauge: "A Foam Pilot Test Aimed at Reducing Gas Inflow in a Production Well at the Oseberg Field," Proceedings of the 8th European IOR Symposium, Vienna, Austria (May 1995).
7. Falls, A.H., G.J. Hirasaki, T.W. Patzek, P.A. Gauglitz, D.D. Miller, and T. Ratulowski: "Development of A Mechanistic Foam Simulator: The Population Balance and Generation By Snap-Off," *SPE*, **3**(3) (1988) 884-892.
8. Patzek, T.W.: "Description of Foam Flow in Porous Media by the Population Balance Approach", *Surfactant-Based Mobility Control: Progress in Miscible-Flood Enhanced Oil Recovery*, D.H. Smith, Editor, American Chemical Society, Washington, D. C., (1988) p. 326-341.
9. Ettinger, R.A. and C.J. Radke: "Influence of Foam Texture on Steady Foam Flow in Berea Sandstone," *SPE*, **7**(1) (1992) 83-90.
10. Chang, S.H., L.A. Owusu, S.B. French, and F.S. Kovarik: "The Effect of Microscopic Heterogeneity on CO<sub>2</sub>-Foam Mobility: Part 2--Mechanistic Foam Simulation," SPE/DOE 20191, Proceedings of the SPE/DOE 7th Symposium on Enhanced Oil Recovery, Tulsa, Oklahoma (April, 1990).
11. Friedmann, F., W.H. Chen, and P.A. Gauglitz: "Experimental and Simulation Study of High-Temperature Foam Displacement in Porous Media," *SPE*, **6**(1) (1991) 37-45.

12. Kovscek, A.R. and C.J. Radke: "Fundamentals of Foam Transport in Porous Media", *Foams in the Petroleum Industry*, L.L. Schramm, Editor., American Chemical Society, Washington, D.C., (1994) p. 115-163.
13. Kovscek, A.R., T.W. Patzek, and C.J. Radke: "A Mechanistic Population Balance Model For Transient and Steady-State Foam Flow in Boise Sandstone," *Chem. Eng. Science*, **50**(23) (1995) 3783-3799.
14. Kovscek, A.R., T.W. Patzek, and C.J. Radke: "Simulation of Foam Transport in Porous Media," SPE 26402, Proceedings of the the 68th Annual Technical Conference of SPE, Houston, TX (October 1993).
15. Chambers, K.T. and C.J. Radke: "Capillary Phenomena in Foam Flow Through Porous Media", *Interfacial Phenomena in Petroleum Recovery*, N.R. Morrow, Editor. , Marcel Dekker Inc., New York, (1991) p. 191-255.
16. Gillis, J.V. and C.J. Radke: "A Dual-Gas Tracer Technique for Determining Trapped Gas Saturation During Steady Foam Flow in Porous Media," SPE 20519, Proceedings of the 65th SPE Annual Technical Conference, New Orleans, LA (September, 1990).
17. Hirasaki, G.J. and J.B. Lawson: "Mechanisms of Foam Flow in Porous Media: Apparent Viscosity in Smooth Capillaries," *SPEJ*, **25**(2) (1985) 176-190.
18. Falls, A.H., J.J. Musters, and J. Ratulowski: "The Apparent Viscosity of Foams in Homogeneous Beadpacks," *SPE*, **4**(2) (1989) 155-164.
19. Ettinger, R.A.: "Foam Flow Resistance in Berea Sandstone," MS. Thesis, University of California, Berkeley (1989)
20. Fergui, A., M. Quintard, H. Bertin, and D. Defives: "Transient Foam Flow in Porous Media: Experiments and Simulation," Proceedings of the 8th European IOR Symposium, Vienna Austria (May 1995).
21. Rossen, W.R.: "Theory of Mobilization Pressure Gradient of Flowing Foams in Porous Media: I. Incompressible Foam," *J. Coll. Interface. Sci.*, **136**(1) (1990) 1-16.
22. Rossen, W.R.: "Theory of Mobilization Pressure Gradient of Flowing Foams in Porous Media: II. Effect of Compressibility," *J. Coll. Interface. Sci.*, **136**(1) (1990) 17-37.
23. Rossen, W.R.: "Theory of Mobilization Pressure Gradient of Flowing Foams in Porous Media: II. Asymmetric Lamella Shapes," *J. Coll. Interface. Sci.*, **136**(1) (1990) 38-53.
24. Rossen, W.R. and P.A. Gauglitz: "Percolation Theory and Mobilization of Foams in Porous Media," *Am. Inst. Chem. Eng. J.*, **37**(8) (1990) 1176-1188.
25. Chou, S.I.: "Percolation Theory of Foam in Porous Media," SPE/DOE 20239, Proceedings of the 7th SPE/DOE Symposium on Enhanced Oil Recovery, Tulsa, OK (April, 1990).
26. Rossen, W.R., Z.H. Zhou, and C.K. Mamum: "Modeling Foam Mobility in Porous Media," SPE 22627, Proceedings of the 66th SPE Annual Technical Conference, Dallas, TX (October 1991).
27. Zhou, Z. and W.R. Rossen: "Applying Fractional Flow Theory to Foam Processes at the Limiting Capillary Pressure," SPE/DOE 24180, Proceedings of the SPE/DOE 8th Symposium on Enhanced Oil Recovery, Tulsa, OK (April 1992).
28. Fisher, A.W., R.W.S. Foulser, and S.G. Goodyear: "Mathematical Modeling of Foam Flooding," SPE/DOE 20195, Proceedings of the 7th SPE/DOE Symposium on Enhanced Oil Recovery, Tulsa, OK (April 1990).
29. Liu, D. and W.E. Brigham: "Transient Foam Flow in Porous Media With the Cat Scanner," DOE/BC 14600-19, U.S. D.O.E. (March, 1992)
30. Patzek, T.W. and N.A. Myhill: "Simulation of the Bishop Steam Foam Pilot," SPE 18786, Proceedings of the SPE California Regional Meeting, Bakersfield, CA (April 1989).
31. Mohammadi, S.S., D.A. Coombe, and V.M. Stevenson: "Test of Steam-Foam Process for Mobility Control in S. Casper Creek Reservoir," *J. Can. Pet. Tech.*, **32**(10) (1993) 49-54.
32. Mohammadi, S.S. and D.A. Coombe: "Characteristics of Steam/Foam Drive Process in Massive Multi-Zone and Thin Single Zone Reservoirs," SPE 24030, Proceedings of the SPE California Regional Meeting, Bakersfield, CA (April 1992).
33. Marfoe, C.H. and H. Kazemi: "Numerical Simulation of Foam Flow in Porous Media," SPE 16709, Proceedings of the 62nd SPE Annual Meeting, Dallas, TX (September, 1987).
34. Mahmood, S.M., S.M. Tariq, and W.E. Brigham: "A Model for Prediction of Recovery and Pressure History for 2-D Displacement of Oil Through Porous Media by Gas/Surfactant," SPE 15076, Proceedings of the the SPE California Regional Meeting, Oakland, CA (April 1986).
35. Kovscek, A.R. and C.J. Radke: "Gas Bubble Snap-Off Under Pressure Driven Flow in Constricted Noncircular Capillaries," *Colloids and Surfaces A: Physicochemical and Engineering Aspects*, **117**(1996) 55-76.
36. Jiménez, A.I. and C.J. Radke: "Dynamic Stability of Foam Lamellae Flowing Through a Periodically Constricted Pore", *Oil-Field Chemistry: Enhanced Recovery and Production Stimulation*, J.K. Borchardt and T.F. Yen, Editors. , American Chemical Society, Washington, D.C., (1989) p. 460-479.
37. Khatib, Z.I., G.J. Hirasaki, and A.H. Falls: "Effects of Capillary Pressure on Coalescence and Phase Mobilities in Foams Flowing Through Porous Media," *SPE*, **3**(3) (1988) 919-926.
38. Aronson, A.S., V. Bergeron, M.E. Fagan, and C.J. Radke: "The Influence of Disjoining Pressure on Foam Stability and Flow in Porous Media," *Colloids and Surfaces A: Physicochemical Eng. Aspects*, **83**(1994) 109-120.
39. Leverett, M.C.: "Capillary Behavior in Porous Solids," *Trans., AIME*, **142**(1941) 152-169.
40. Bretherton, F.P.: "The Motion of Long Bubbles in Tubes," *J. Fluid Mech.*, **10**(1961) 166-188.
41. Wong, H., C.J. Radke, and S. Morris: "The Motion of Long Bubbles in Polygonal Capillaries: I. Thin Films," *J. Fluid Mech.*, **292**(1995) 71-95.
42. Wong, H., C.J. Radke, and S. Morris: "The Motion of Long Bubbles in Polygonal Capillaries: II. Drag, Fluid Pressure, and Fluid Flow," *J. Fluid Mech.*, **292**(1995) 95-110.
43. Stone, H.L.: "Probability Model for Estimating Three-Phase Relative Permeability," *J. Pet. Tech.*, **22**(2) (1970) 214-218.
44. Bernard, G.G., L.W. Holm, and L.W. Jacobs: "Effect of Foam on Trapped Gas Saturation and on Permeability of Porous Media to Gas," *SPEJ*, **5**(4) (1965) 295-300.
45. Holm, L.W.: "The Mechanism of Gas and Liquid Flow Through Porous Media in the Presence of Foam," *Soc. Pet. Eng. J.*, **8**(4) (1968) 359-369.
46. Sanchez, J.M., R.S. Schechter, and A. Monsalve: "The Effect of Trace Quantities of Surfactant on Nitrogen/Water Relative Permeabilities," SPE 15446, Proceedings of the 61st SPE Annual Technical Conference, New Orleans, LA (October, 1986).
47. Huh, D.G. and L.L. Handy: "Comparison of Steady- and Unsteady-State Flow of Gas and Foaming Solution in Porous Media," *Soc. Pet. Eng. Res. Eng.*, **4**(1) (1989) 77-84.
48. De Vries, A.S. and K. Wit: "Rheology of Gas/Water Foam in the Quality Range Relevant to Steam Foam," *Soc. Pet. Eng. Res. Eng.*, **5**(2) (1990) 185-192.

49. Adenekan, A.E., T.W. Patzek, and K. Pruess: "Modeling of Multiphase Transport of Multicomponent Organic Contaminants and Heat in the Subsurface: Numerical Model Formulation," *Water Resources Research*, **29**(11) (1993) 3727-3740.
50. Pruess, K.: "TOUGH2--A general-purpose simulator for multiphase fluid and heat flow," Rep. LBL-29400 , Lawrence Berkeley Lab. (September 1991)
51. Pruess, K.: "TOUGH Users's Guide," Rep NUREG/CR-4 645 , Nucl. Reg. Commision, Washington D.C. (1987)
52. Narasimhan, T.N. and P.A. Witherspoon: "An Integrated Finite Difference Method for Analyzing Fluid Flow in Porous Media," *Water Resources Research*, **12**(1) (1976) 57-64.
53. International Formulation Committee: "A Formulation of the Thermodynamic Properties of Ordinary Water Substance," IFC Secretariat, Düsseldorf, Germany (1967)
54. Patzek, T.W.: "Field Application of Steam Foam for Mobility Improvement and Profile Control," *SPE RE May*(1996) 79-85.
55. Friedmann, F. and J.A. Jensen: "Some Parameters Influencing the Formation and Propagation of Foams in Porous Media," SPE 15087, Proceedings of the SPE California Regional Meeting, Oakland, CA (April, 1986).
56. Persoff, P., C.J. Radke, K. Pruess, S.M. Benson, and P.A. Witherspoon: "A Laboratory Investigation of Foam Flow in Porous Media at Elevated Pressure," *SPE RE*, **6**(3) (1991) 365-371.

#### **SPEJ**

**A.R. Kovscek** SPE, is an assistant professor of petroleum engineering at Stanford U., Department of Petroleum Engineering, Stanford University, Stanford, CA 94305-2220, email: kovscek@pangea.stanford.edu. His interests include fluid and heat flow in tight fractured rocks and foams for mobility control of gas injection processes. Before joining Stanford, he worked in the Earth Sciences Division of Lawrence Berkeley National Laboratory. He holds a Ph. D. from the University of California, Berkeley and a B.S. from the University of Washington. Both degrees are in Chemical Engineering.

**T. W. Patzek**, SPE, is an associate professor of petroleum engineering at the U. of California, Department of Materials Science and Mineral Engineering, 591 Evans Hall #1760 Berkeley, CA 94720-1760, email: patzek@patzek.berkeley.edu. Previously, he worked for Shell Western E&P and in the Enhanced Recovery Research Department of Shell Development. His research activities include 3D modeling of foam flow in porous media with the population balance method; diffusion stability of stationary foams in porous media; the development of a finite difference simulator of multicomponent, multiphase, nonisothermal flow in porous media; the use of steam to clean hydrocarbon spills; micro-earthquake imaging of massive hydrofractures; neural network models of fluid injection and withdrawal in tight rock; and inverse modeling of steam injection into diatomite. He holds a Ph. D. degree in Chemical Engineering from Silesian Technical U., Poland.

**C.J. Radke**, SPE, is a professor of chemical engineering at the U. of California, Department of Chemical Engineering, 101E Gilman Hall, Berkeley, CA 94720, email: radke@cchem.berkeley.edu.